PHYSICAL REVIEW A **109**, 043530 (2024)

Generation, manipulation, and detection of snake-state trajectories of a neutral atom in a ring cavity

Poornima Shakya,[1] Nishant Dogra,[2] and Sankalpa Ghosh[1]
[1]*Department of Physics, Indian Institute of Technology Delhi, New Delhi 110016, India*
[2]*Physics Department, Cavendish Laboratory, Cambridge CB3 0HE, United Kingdom*

(Received 16 April 2023; revised 2 March 2024; accepted 1 April 2024; published 26 April 2024)

We propose a setup to create and detect the atomic counterpart of snake-state trajectories which occur at the interface where the magnetic field reverses direction. Such a synthetic magnetic field is generated by coupling two counterpropagating modes of a ring cavity to a two-level atom. The spatial distribution and the strength of the induced magnetic field are controlled by the transverse- mode profile of the cavity modes and the number of photons in the two modes, respectively. By analyzing the atomic motion in such a magnetic field while including the cavity back-action, we find that the atom follows snake-state trajectories which can be nondestructively detected and reconstructed from the phase and the intensity of the light field leaking from the cavity. We finally show that the system parameters can be tuned to modify the transport properties of the snake states and even amplify the effect of cavity feedback, which can completely alter their topology.

DOI: 10.1103/PhysRevA.109.043530

I. INTRODUCTION

Laser-induced synthetic gauge fields, realized by coupling different internal atomic states [1–18], have provided a unique tool for extremely well controlled and tunable ultracold atomic systems [19–22]. Such gauge fields have paved the way for the realization and investigation of phenomena like the quantum Hall effect [23–25], spin-orbit coupling [15–18], and topological superfluidity [2,26,27], as well as quantum simulation of fundamental topological models like the Hofstadter model [5,13,14,28] and Haldane model [29]. As opposed to static gauge fields, which are described as externally imposed potentials in the atomic Hamiltonian, dynamical gauge fields additionally include the feedback from atomic dynamics and are a crucial ingredient of many fundamental gauge theories [30–35]. One way to generate such feedback is to couple an ultracold atomic system to a single- or multimode optical cavity in which the atomic wave function and its dynamics affect the phase and the intensity of the intracavity field and, in turn, the cavity field provides dynamical feedback on the atomic state. Such systems have been used to study phenomena such as Dicke superradiance in single-pump [36] and two-pump [37] systems, continuous supersolidity [38], dynamical spin-orbit coupling [39], and self-oscillating topological pumps [40] and are predicted to generate an artificial Meissner effect [41], quantum magnetism [42,43], topological superradiant states [44–48] and self-organized chiral edge states [49–54] (see [55,56] for a complete list).

An important motivation for realizing synthetic gauge fields is to create topologically nontrivial quantum phases which support edge modes [47,49] that are resilient to scattering from defects and disorders and can be useful for topological quantum computation [57,58]. One-dimensional snake trajectories that occur at the boundaries separating different magnetic or charge domains provide a convenient way of realizing such protected modes in solid-state electronic systems [59–70]. References [66–70] noted that such current-carrying magnetic edge states can couple differently with the current-carrying electrostatic edge states in the quantum Hall regime and change the conductivity. Such states were experimentally observed in a two-dimensional electron gas [60] and graphene [61,62] by measuring transport properties such as current and conductance. However, real-time detection of such states is difficult in condensed-matter experiments and is crucial for their complete characterization to understand their role in conductivity enhancement in electronic systems [71–77].

In this paper, we theoretically demonstrate that the atomic analog of such snake states can be realized using an atom-cavity coupled system in a more efficient and versatile way than their electronic counterpart. We consider a two-level atom coupled to two counterpropagating and orthogonally polarized running-wave modes of a high-finesse ring cavity. Using a dressed-state approach, we show that a nonuniform synthetic magnetic field, with strength proportional to the difference in the photon number in the two cavity modes, can be generated. The spatial structure of this magnetic field is governed by the transverse-mode profile of the cavity modes, and it changes sign about a point of symmetry for a Gaussian mode profile. By solving semiclassical equations of motion of the system in the presence of such a magnetic field, we show that the atom follows a snake-state trajectory. Not only does the presence of the cavity add a dynamic character to the generated artificial magnetic field, but an analysis of the cavity transmission spectrum also allows real-time monitoring of the atomic state in a nondestructive way. Here, we show that the phase and intensity of the light in the two cavity modes can be used to reconstruct the snake-state trajectory in real time, with a minimal effect of the cavity back-action [78]. This is one of the key results in this paper. We further illustrate that we can manipulate the conductance properties of the snake states (amplitude and direction) by tuning the initial atomic speed orthogonal to the direction of transport, the external pumping strength of the two cavity modes, and the strength of atom-cavity coupling. Finally, we show that the effect of cavity back-action can be enhanced by making the (average) photon numbers in the two cavity modes comparable, which leads to the destruction of the topology of the snake states and results in the formation of states with more complex spatial trajectories. Our work will pave the way for long-distance transport in atomtronics via snake states, which could have technological applications in the fields of quantum computation and quantum information processing [79–82].

II. SYSTEM HAMILTONIAN

We consider a single two-level atom with internal states $|g\rangle$ and $|e\rangle$ coupled to two counterpropagating running-wave modes of a ring cavity, as shown in Fig. 1(a). The two cavity modes are orthogonally polarized and are pumped on axis with pump strengths η_1 and η_2. The total Hamiltonian describing the coupled atom-cavity system in the rotating frame of the pump field space [83] can be written as (see Appendix A for details)

$$\hat{H}_{\mathrm{RF}} = \hat{H}_0 + \hat{H}_I, \tag{1}$$

where

$$\begin{aligned}\hat{H}_0 &= \frac{\hat{P}^2}{2m_a}\hat{\mathbb{I}},\\ \hat{H}_I &= -\frac{\hbar\Delta_a\hat{\sigma}_z}{2} - \hbar\Delta_c(\hat{a}_1^\dagger\hat{a}_1 + \hat{a}_2^\dagger\hat{a}_2)\\ &\quad + \hbar\eta_1(\hat{a}_1 + \hat{a}_1^\dagger) + \hbar\eta_2(\hat{a}_2 + \hat{a}_2^\dagger)\\ &\quad + \hbar[g_1(y)\hat{\sigma}^+\hat{a}_1 e^{ikx} + g_2(y)\hat{\sigma}^+\hat{a}_2 e^{-ikx}\\ &\quad + g_1(y)\hat{\sigma}^-\hat{a}_1^\dagger e^{-ikx} + g_2(y)\hat{\sigma}^-\hat{a}_2^\dagger e^{ikx}].\end{aligned}$$

$\hat{H}_0$ represents the kinetic energy of the atom, where $\hat{\mathbb{I}} = |g\rangle\langle g| + |e\rangle\langle e|$ is the identity operator in the internal two-dimensional Hilbert space of the atom, m_a is the atom mass, and $\vec{r}$ and $\vec{P}$ are the atomic center-of-mass coordinate and momentum, respectively. $\hat{H}_I$ represents the interaction Hamiltonian of the system, where ω_a is the atomic resonance frequency, ω_p is the pump frequency, ω_c is the cavity resonance frequency, $\Delta_a = \omega_p - \omega_a$ is the atom-pump detuning, and $\Delta_c = \omega_p - \omega_c$ is the cavity-pump detuning. $\hat{\sigma}_z = |e\rangle\langle e| - |g\rangle\langle g|$ is the Pauli matrix, and $\hat{\sigma}^+$ and $\hat{\sigma}^-$ are the atomic raising and lowering operators. $g_{1(2)}(y) = g_{10(20)}e^{-y^2/w_0^2}$ is the atom-photon coupling, with w_0 being the waist of the two cavity modes and $g_{10(20)} = \frac{-\vec{d}\cdot\hat{e}_{y(z)}}{\hbar}\sqrt{\frac{\hbar\omega_c}{2\epsilon_0 V}}$, with $|g_{10}| = |g_{20}| = g_0$. $\hat{a}_1$ and $\hat{a}_2$ are the annihilation operators for the two cavity modes with respective spatial mode profiles of the forms $e^{ikx}e^{-y^2/w_0^2}$ and $e^{-ikx}e^{-y^2/w_0^2}$, with $k = 2\pi/\lambda_p$. Following a mean-field approach, we assume that the cavity fields can be described by a coherent state of the form $|\alpha_1, \alpha_2\rangle = |\alpha_1\rangle|\alpha_2\rangle$, with $\hat{a}_{1(2)}|\alpha_{1(2)}\rangle = \alpha_{1(2)}|\alpha_{1(2)}\rangle$ and $n_{1(2)} = |\alpha_{1(2)}|^2$ being the average photon number in cavity mode 1 (2). The phase associated with the cavity field in mode 1 (2) is $\alpha_{1(2)} = \sqrt{n_{1(2)}}e^{i\phi_{1(2)}}$. We assume that all the dynamics take place in the x-y plane, so we neglect the z coordinate in different expressions.

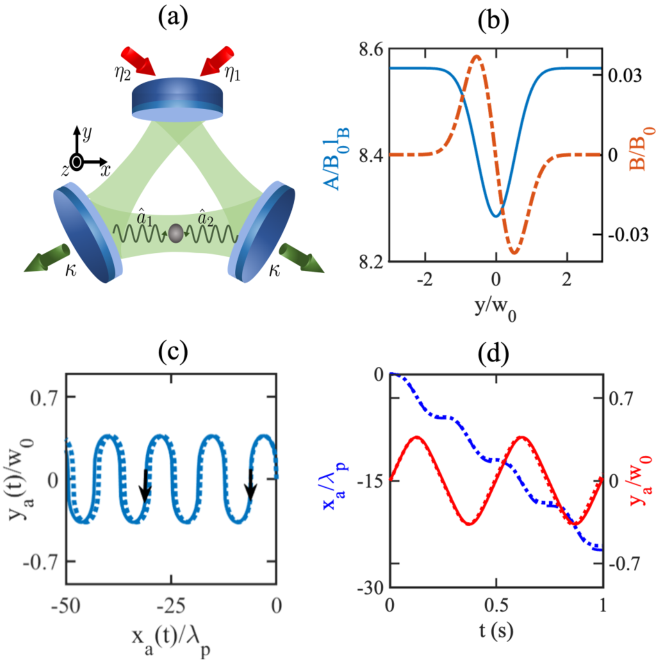

FIG. 1. (a) Schematic of a single two-level atom trapped inside a ring cavity with two counterpropagating running-wave modes which are orthogonally polarized and are described by the photon annihilation operators $\hat{a}_1$ and $\hat{a}_2$. The two modes are respectively pumped with strengths η_1 and η_2. κ is the cavity decay rate. For (b)–(d) $\eta_1 \approx 2\pi \times 52$ MHz, and $\eta_2 = 0$, which gives time-averaged photon numbers in the two cavity modes of $\langle n_1\rangle \approx 342$ and $\langle n_2\rangle \approx 8$. (b) Vector potential A (blue solid curve) and magnetic field B (orange dash-dotted curve) as a function of y. B_0 and l_B are, respectively, the natural magnetic field and magnetic length scales of the system, and w_0 is the waist size of the cavity modes (see text). (c) The snake-state trajectory of the atom in the x-y plane, with λ_p being the pump wavelength. The black arrows indicate the direction of increasing time. (d) The x position x_a (blue dashed curve) and y position y_a (red solid curve) of the atom as a function of time t. The dotted curves in (c) and (d) show the atomic trajectory, x position, and y position for fixed photon numbers $\langle n_1\rangle$ and $\langle n_2\rangle$ in the two cavity modes and thus exclude cavity back-action.

We diagonalize the interaction Hamiltonian $\hat{H}_I$ in the space spanned by the atom-photon bare states, namely, $|e, \alpha_1, \alpha_2\rangle$ and $|g, \alpha_1, \alpha_2\rangle$, and obtain eigenstates that are called dressed states $|D_{1(2)}\rangle$ for the coupled atom-photon system, with eigenenergies $E_{1(2)}$; see Appendix A for details. Under adiabatic approximation [1,84–93], we limit the system dynamics in the eigenspace of the lowest-energy dressed state $|D_1\rangle$ and obtain the following equation for the evolution of the corresponding wave function ψ_1 (see Appendix A):

$$\begin{aligned}i\hbar\frac{\partial}{\partial t}\psi_1(\vec{r}, t) &= H_S\psi_1(\vec{r}, t)\\ &= \left[\frac{1}{2m_a}\{(\vec{p} - \vec{\mathbf{A}}_{1,1})^2 + |\vec{\mathbf{A}}_{2,1}|^2\} + E_1\right]\psi_1(\vec{r}, t).\end{aligned} \tag{2}$$

Here, $\vec{\mathbf{A}}_{1,1}$ acts as a synthetic vector potential, while $\vec{\mathbf{A}}_{2,1}$ contributes to the synthetic scalar potential term, given by $W = \frac{1}{2m_a}|\vec{\mathbf{A}}_{2,1}|^2$. The last term in Eq. (2), E_1, acts as a deep-trapping potential for the atomic center-of-mass motion. In the next section, we will explain why the important dynamics of the system are governed only by the vector potential $\vec{\mathbf{A}}_{1,1}$. The scalar potential, the vector potential, and the corresponding magnetic field obtained here depend on the difference in the photon number in the two cavity modes, which dynamically depends on the position of the atom.

The full expression for the cavity-induced synthetic vector potential in Eq. (2) is given as

$$\begin{aligned}\vec{\mathbf{A}}_{1,1} &= i\hbar\langle D_1|\vec{\nabla}|D_1\rangle = A_x(y)\hat{x}\\ &= \frac{2\hbar k g^2(y)(n_1-n_2)}{G(G+\Delta_a)}\hat{x},\end{aligned} \tag{3}$$

where $G = \sqrt{\Delta_a^2 + 4g^2(y)(n_1+n_2)}$. The corresponding synthetic magnetic field is

$$\vec{B} = -\frac{\partial A_x}{\partial y}\hat{z} = B_0\frac{y}{w_0}\frac{\Delta_a}{G^3}4g^2(y)(n_1-n_2)\hat{z}, \tag{4}$$

where $B_0 = \frac{\hbar k}{w_0}$ defines the natural scale of the synthetic magnetic field with dimensions $[MT^{-1}]$ and the corresponding synthetic magnetic length is given by $l_B = \sqrt{\frac{\hbar}{B_0}}$. Here, we observe that both the vector potential and the magnetic field scale with the difference in the photon numbers in the two cavity modes, n_1 and n_2, and thus can be tuned via $\eta_{1(2)}$, Δ_c, and g_0. The expression for the scalar potential W is

$$W = \frac{\hbar^2k^2}{2m_a}(G^2-\Delta_a^2)\left[\left(\frac{y\Delta_a}{kw_0^2G^2}\right)^2 + \frac{1}{4G^2}\right], \tag{5}$$

where $E_R = \frac{\hbar^2k^2}{2m_a}$ is the recoil energy of the atom. We provide the spatial variation of the scalar potential in Appendix B 1. The parameters considered in this work are for ^{87}Rb: $m_a = 1.4\times10^{-25}$ kg, $\kappa = 2\pi\times650$ kHz, $\Delta_c = -5\kappa$, $g_0 = 2\pi\times 50$ MHz, $\lambda_p = 780.25$ nm, $\Delta_a \approx -2\pi\times4.9$ GHz, $w_0 = 10$ µm, $\eta_1 = 80\kappa$, and $\eta_2 = 0$. $\Gamma = 2\pi\times6$ MHz is the spontaneous emission rate of the atom. For these parameters, we get $B_0 = 8.48\times10^{-23}$ kg/s and $l_B = 1.1$ µm. Using the magnetic length, the natural velocity scale of the system is $v_0 = \hbar/(m_a l_B) = 655$ µm/s. As $v_0 \ll \hbar k/m_a = 5.9$ mm/s, the adiabatic approximation, which implies that when the atom moves slowly enough, it remains in the state in which it started ($|D_1\rangle$ in our case), is justified. The presence of any external trap does not impact the shape of the resulting magnetic field; see Appendix B 2 for details.

In Fig. 1(b), we plot the vector potential and the magnetic field. The vector potential $A_x(y)$ has a symmetric Gaussian profile given by the cavity-mode shape. The corresponding magnetic field B_z scales linearly for $|y| \ll w_0$ with a slope proportional to $n_1 - n_2$ and reverses direction about $y = 0$. B_z achieves its maximum magnitude at $|y| = 0.5w_0$ and decays smoothly to zero for $|y| > 0.5w_0$. In the subsequent sections, we discuss the dynamics of a single atom in the presence of such nonuniform magnetic fields using a semiclassical method. It may be pointed out that such an inhomogeneous synthetic gauge field can be created using different methods [94,95]. However, coupling to a ring cavity allows for nearly nondestructive monitoring of the resultant dynamics, as we show below.

III. TRAJECTORIES OF A SINGLE ATOM AND BACK-ACTION OF THE CAVITY FIELDS

We now obtain the following semiclassical equation of motion for the atom due to the adiabatic following of the lowest-energy dressed state [96,97]:

$$m_a\frac{d\vec{v}}{dt} = -\vec{\nabla}E_1 - \vec{\nabla}W(\vec{r}) + \vec{v}\times\vec{B}(\vec{r}). \tag{6}$$

We want to isolate the effect of the $B(y)$ term on the atomic trajectory, so we neglect the $E_1 + W$ contribution. In a multilevel atom, the effect of $E_1 + W$ can be eliminated by the proper choice of the pump wavelength. So the two components of the equation of motion become

$$m_a\frac{d^2x}{dt^2} = B(y)\frac{dy}{dt}, \tag{7a}$$

$$m_a\frac{d^2y}{dt^2} = -B(y)\frac{dx}{dt}. \tag{7b}$$

The solution of the above equations gives us the atomic trajectory. To find the magnetic field, we need to additionally evaluate the number of photons in the two cavity modes, which depends on the atomic position itself. As $\kappa \gg \hbar k^2/2m_a, \hbar/(2m_a l_b^2)$, we assume that the cavity field is always in a steady state and adiabatically follows the atomic motion. We thus obtain the following expressions for the two cavity fields:

$$\begin{aligned}\alpha_{1(2)} &= \langle\hat{a}_{1(2)}\rangle = \langle D_1|\hat{a}_{1(2)}|D_1\rangle\\ &= \frac{i\eta_{1(2)}(i\bar{\Delta}_c - \bar{\kappa}) + i\eta_{2(1)}(iU+\gamma)e^{\mp 2ikx_a(t)}}{(i\bar{\Delta}_c-\bar{\kappa})^2 - (iU+\gamma)^2},\end{aligned} \tag{8}$$

where $U_0 = \frac{\Delta_a g_0^2}{\Delta_a^2+4\Gamma^2} \approx \frac{g_0^2}{\Delta_a} \approx 2\pi\times500$ kHz, $U = U_0 e^{-2y_a^2(t)/w_0^2}$, $\gamma_0 = \frac{2\Gamma g_0^2}{\Delta_a^2+4\Gamma^2} \approx \frac{2\Gamma g_0^2}{\Delta_a^2} \approx 2\pi\times1.2$ kHz, $\gamma = \gamma_0 e^{-2y_a^2(t)/w_0^2}$, $\bar{\Delta}_c = \Delta_c - U$, and $\bar{\kappa} = \kappa + \gamma$ (the numerical values correspond to the parameters noted in the previous section). To obtain the atomic trajectory in the x-y plane, we solve Eqs. (7a) and (7b) simultaneously with Eq. (8). We take the initial velocities $v_{x0} = 0$ and $v_{y0} = 0.06v_0$ and initial positions $x_{a0} = 0$ and $y_{a0} = 0$. We plot $y_a(t)$ as a function of $x_a(t)$ in Fig. 1(c) and realize that the particle drifts in the $-x$ direction while oscillating in the y direction, which is a snake-state trajectory. The origin of such a trajectory is the following: The atom experiences a magnetic field with a finite slope which reverses direction around $y = 0$, and thus, for $v_{x0} = 0 \neq v_{y0}$, a finite particle current is generated along the $-x$ direction [59,98]. The instantaneous radius of curvature $r(y)$ for the particle trajectory in a synthetic magnetic field is inversely proportional to the strength of the magnetic field: $r(y) \propto \frac{1}{B(y)}$. Therefore, for a large (small) magnitude of the magnetic field and thus large (small) $|y|$, the particle will trace a trajectory with a small (large) radius of curvature, resulting in the peculiar snake-state trajectory in the x-y plane [59,98]. The quantum fluctuations of the motion could give rise to a velocity distribution resulting in broader

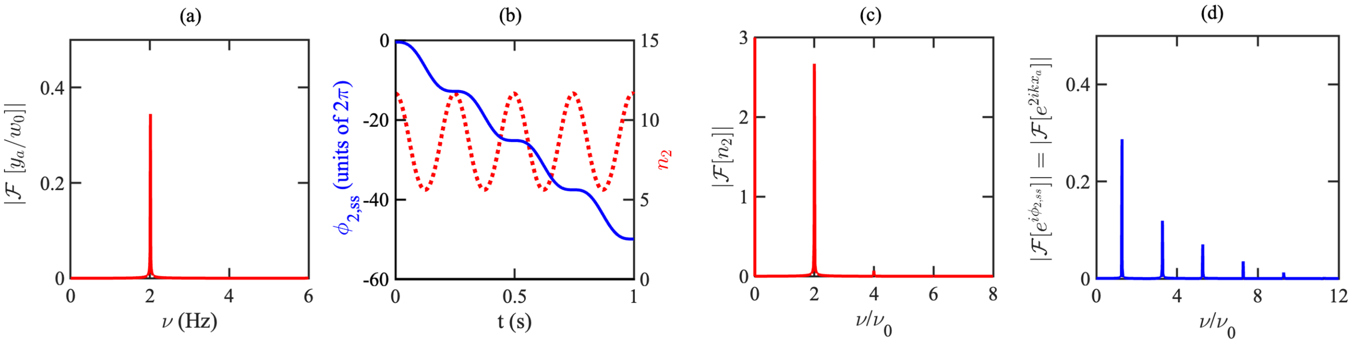

FIG. 2. (a) Fourier transform for y_a/w_0, which shows a peak at $\nu_0 \approx 2$ Hz. (b) Photon number n_2 (red dotted curve) and the corresponding phase $\phi_{2,\mathrm{ss}}$ (blue solid curve) in cavity mode 2 as a function of time t. (c) Fourier transform of n_2, which shows peaks at $2\nu_0$, $4\nu_0$, $6\nu_0$, and so on. (d) Fourier transform of $e^{i\phi_{2,\mathrm{ss}}}$, which overlaps with the Fourier transform of e^{2ikx_a}.

snake trajectories. However, with the presence of cavity noise and the finite lifetime of the excited state, such effects might be suppressed.

We plot $x_a(t)$ and $y_a(t)$ as a function of t in Fig. 1(d). Along the y direction, the particle oscillates periodically about $y = 0$ at a fixed frequency, as illustrated by the corresponding Fourier transform (denoted by the symbol $\mathcal{F}$) in Fig. 2(a). Along the x direction, the particle has a finite average speed $\langle v_x \rangle$, where the notation $\langle S \rangle$ implies the time-averaged value of a periodically oscillating quantity S. The dashed curves in Figs. 1(c) and 1(d) illustrate the particle trajectories when the numbers of photons in the two cavity modes are fixed to the time-averaged values given by Eq. (8); see Fig. 2 for the full time evolution of the cavity fields. We observe that the cavity feedback minimally affects the snake-state trajectory of the particle, and in general, this is true when $\langle n_1 \rangle$ and $\langle n_2 \rangle$ are very different from each other, as we illustrate in Sec. VI. The analytical formula for the period of the y trajectory can be estimated as

$$y_{\mathrm{period}} = \frac{1}{4\pi}\sqrt{\frac{m_a}{B_0 v_{y0}}}. \tag{9}$$

The above formula is obtained by approximating the Gaussian magnetic field by a linear spatially varying field for $y_a < w_0$ [see Fig. 1(b)]. This is valid for $y_a^{\mathrm{pp}} \leqslant w_0$, and for $y_a^{\mathrm{pp}} \geqslant w_0$, the linear approximation of the Gaussian field breaks down. This gives us an idea about the parameters that affect the period of the snake trajectory and hence the frequency of the emitted photons. The pump wavelength λ_p, the cavity waist mode w_0, and the initial velocity of the atom along the y direction v_{y0} can be used to control the period of the trajectory. For small initial velocities, the change in the output photon number is very small, and hence, the detection of the trajectories will be difficult. The magnetic-field dependence in the period also brings into the picture the laser fluctuations and the fluctuations in the output photon numbers n_1 and n_2, as can be seen in Eq. (4). We will discuss the effect of the velocity and laser fluctuations in Sec. V, where we calculate the signal-to-noise ratio as a function of initial velocity and pump strength. However, since the equations of motion do not have an exact analytical solution, the numerically obtained period of the oscillating trajectory can vary from the value obtained from the above formula. In Appendix D 1, we show the numerical plot for the frequency of the snake trajectory in Fig. 11. We also plot the frequency obtained from y_{period} in Eq. (9) in Fig. 11(a).

IV. CAVITY-BASED DETECTION OF THE SNAKELIKE TRAJECTORIES

To probe the snake-state trajectory, we now look at the time evolution of the cavity field of mode 2, $\alpha_2 = \sqrt{n_2}e^{i\phi_{2,\mathrm{ss}}}$, where the subscript ss in $\phi_{2,\mathrm{ss}}$ denotes the snake-state phase. This is illustrated in Fig. 2(b). We realize that the time variations of the phase $\phi_{2,\mathrm{ss}}$ and photon number n_2 are qualitatively similar to x_a and y_a, respectively. We can understand such behavior as follows: The atom moving in the $-x$ direction absorbs a photon from cavity mode 1 and emits it into the counterpropagating mode (cavity mode 2). This decreases the atom's momentum by $2\hbar k$, and correspondingly, the e^{i2kx_a} phase is imprinted on the photon scattered into cavity mode 2, thus mapping x_a on phase $\phi_{2,\mathrm{ss}}$. The periodic atomic oscillation along the y direction modulates the atom-cavity coupling $g(y)$, which has a Gaussian form (centered at $y = 0$), and thus, there is a periodic oscillation of n_2, which links y_a to n_2. This can be easily seen via Eq. (8) by assuming $|\Delta_c| \gg (\kappa, U_0) \gg \gamma_0$ (which is true for our case), and we obtain

$$\alpha_2 \approx \frac{-\eta_1 g_0^2 e^{-2y_a^2(t)/w_0^2} e^{2ikx_a(t)}}{\Delta_a(i\bar{\Delta}_c - \bar{\kappa})^2}, \tag{10}$$

which shows that $n_2 \propto e^{-4y_a^2(t)/w_0^2}$ and $\phi_{2,\mathrm{ss}} \approx 2kx_a(t)$ (excluding constants coming from other prefactors). We would like to point out that the above expression is obtained while ignoring the Doppler shift, and more details about this aspect are provided later in this section. For a quantitative comparison, we look at the Fourier transforms of various quantities. The Fourier transform of y_a in Fig. 2(a) shows a nearly monochromatic response at $\nu_0 \approx 2$ Hz. Correspondingly, the Fourier transform of n_2 in Fig. 2(c) shows peaks at even multiples of ν_0, with $2\nu_0$ being the most dominant one. The factor of 2 arises because $g(y)$ decreases for both positive and negative y [see Eq. (10)]. The peak at zero frequency appears because the atom-cavity coupling leads to the scattering of photons into cavity mode 2 even when the particle is stationary. We also note that the pump frequency ω_p is $\sim 2\pi \times 384$ THz [the system Hamiltonian in Eq. (1) is written in the rotating frame of the pump field], and we are looking for a small modulation of a few hertz ($\sim$4 Hz) on top of this frequency. Such a modulation can be measured by a heterodyne measurement of a portion of the on-axis pump laser interfering with the cavity output field. This measurement needs to be done with a laser with a very narrow linewidth (less than 1 Hz), which is within reach of available technologies. The output signal at $2\nu_0 \approx 4$ Hz corresponds to a temperature of ∼0.2 nK, which is quite low. We can use a weakly out-coupled atom laser to generate a very low temperature atomic beam of atoms such that, on average, only one atom passes through the cavity at a time. Alternatively, we can use a Bose-Einstein condensate from which single atoms with known trajectories are extracted using interfering (Bragg) laser beams. We also observe a nonlinear time evolution of x_a as revealed via a series of frequency peaks that are integer multiples of a fundamental frequency in the Fourier transform of e^{2ikx_a} which overlaps exactly with the Fourier transform of $e^{i\phi_{2,\mathrm{ss}}}$ [see Fig. 2(d)]. Thus, the cavity field α_2 can be used to reconstruct the snake-state trajectories; see Appendix C 1 for a full reconstruction. In Appendix C 2, we show the time evolution of n_1 and ϕ_1 and observe that they also predominantly oscillate at frequency $2\nu_0$ with the caveat that the oscillation amplitude normalized by the corresponding time-average value is much smaller. With a heterodyne measurement and external locking of the laser frequency (e.g., to a reference vapor cell), the drift of the laser frequency can be minimized, and the laser linewidth can be reduced. With available experimental techniques, the laser intensity can be stabilized to the 1% level or below. We also note from Fig. 2(b) that the change in the number of photons in the cavity during the snake-state evolution is close to 100%, which makes it easier to detect.

Additionally, we would like to point out that the effect of Doppler shift on the spontaneous emission from an atom moving in a linear single-mode Fabry-Pérot cavity and its effect on the resulting transmission spectrum [99] are also a relevant issue since the atoms are moving in a complex snake-state trajectory. Full treatment of this is somewhat beyond the scope of the current paper, and it is also complicated by the fact that we consider a ring-cavity structure in which a photon emitted by one cavity mode is absorbed by another cavity mode. Nevertheless, we include a brief analysis of this issue in Appendix C 3 by generalizing the treatment given in [100].

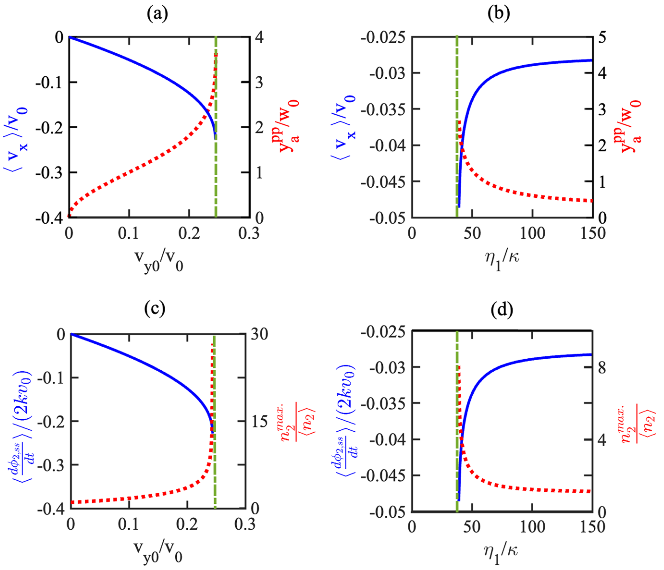

FIG. 3. Average drift velocity $\langle v_x \rangle$ (blue solid curve) and peak-to-peak y_a variation y_a^{pp} (red dotted curve) as a function of (a) the initial velocity v_{y0} (with $\eta_1 = 80\kappa$ and $\eta_2 = 0$) and (b) the pump strength η_1 (with $v_{y0} = 0.06v_0$ and $\eta_2 = 0$). Here, v_0 is a natural velocity scale of the system (see text), w_0 is the cavity-mode waist, and the initial speed along the x direction is fixed to zero. The normalized maximum photon number in cavity mode 2 $n_2^{\max}/\langle n_2 \rangle$ (red dotted curve) and the average time derivative of the corresponding phase $\langle d\phi_{2,\mathrm{ss}}/dt \rangle$ (blue solid curve) are shown in (c) as a function of v_{y0} and in (d) as a function of η_1. The vertical dash-dotted green lines mark the boundary where the snake-state trajectory ceases to exist, and the particle is not trapped along the y direction.

V. MANIPULATION OF SNAKE STATES

Next, we discuss how the snake-state trajectories can be manipulated from the perspective of one-dimensional transport along the x direction. We quantify such transport by two properties: the average drift velocity $\langle v_x \rangle$, which is proportional to the particle conductivity along the x direction, and the peak-to-peak amplitude y_a^{pp} of y_a, which signifies the deviation from a purely one-dimensional transport. We choose two tuning parameters: the initial speed v_{y0} of the atom and the pump strength η_1. As shown in Fig. 3(a), we observe an increase in $\langle v_x \rangle$ (blue solid curve) accompanied by an increase in y_a^{pp} (red dotted curve) when v_{y0} is increased. On the other hand, both these trends are reversed when we instead increase η_1, as depicted in Fig. 3(b). Such behavior can be understood from a basic Lorentz force picture, noting that $|B(y)| \propto \eta_1^2$. Above (below) a critical v_{y0} (η_1), the atom cannot be trapped along the y direction by the synthetic magnetic field, and the snake-state trajectory picture breaks down. This boundary is marked by the vertical dash-dotted green lines in Fig. 3. The initial velocity of the atom v_{y0} can be controlled either by trapping the atom in an optical tweezer and then spatially accelerating the tweezer or by using a thermal atomic beam which has a specific distribution of speeds.

Figures 3(c) and 3(d) show the maximum photon number variation $n_2^{\max}$ in cavity mode 2 normalized by $\langle n_2 \rangle$ and the average time variation of the corresponding phase $\langle d\phi_{2,\mathrm{ss}}/dt \rangle$ as a function of v_{y0} and η_1. We observe that these two quantities mimic the behavior of y_a^{pp} and $\langle v_x \rangle$, and thus, the snake-state trajectories can be mapped on the cavity field for a wide range of parameters. Beyond the critical points where the particle is not trapped, the photon number n_2 decays to zero as the particle leaves the cavity mode. In Appendix D 1, we provide simple scalings of various quantities as a function of our tuning parameters and give some examples of the time evolution of particle properties and cavity fields for different initial conditions. Finally, we note that we have assumed that the initial position of the particle $y_{a0} = 0$ in all the examples presented here. For $|y_{a0}| \approx w_0$, we find that the particle performs normal (cyclotron) orbits similar to those in a homogeneous magnetic field, which can also be mapped on the cavity field of mode 2; see Appendix D 2 for details.

Next, we look at the feasibility of detecting the number of photons leaking from the cavity from the shot-noise point of view. We look at the signal-to-noise ratio (SNR) to

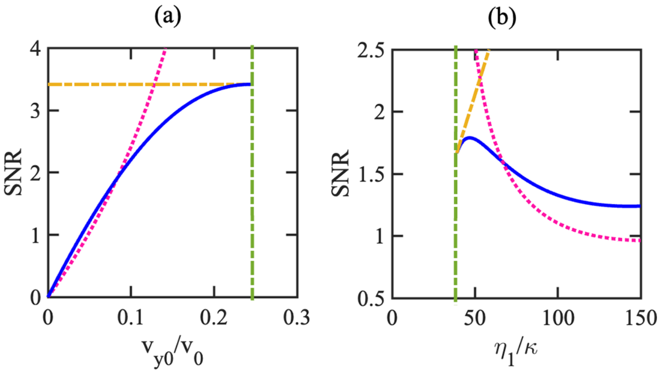

FIG. 4. Signal-to-noise ratio (SNR) as a function of (a) the initial velocity v_{y0} (with $\eta_1 = 80\kappa$ and $\eta_2 = 0$) and (b) the pump strength η_1 (with $v_{y0} = 0.06v_0$ and $\eta_2 = 0$). The blue solid curve shows the numerically obtained SNR. The yellow dash-dotted curve represents the analytical approximation of the SNR for $y_a^{\mathrm{pp}} \gg w_0$, and the magenta dotted curve represents the analytical approximation of the SNR for $y_a^{\mathrm{pp}} \ll w_0$, as discussed in Sec. V. The green dash-dotted vertical lines represent the boundaries where the snake-state-trajectory picture breaks down.

distinguish the maximum (n_2^{max}) and minimum (n_2^{min}) photon numbers and define SNR as S/N, where the signal S is $S = n_2^{\mathrm{max}} - n_2^{\mathrm{min}}$. The shot noise associated with this signal is $N = \sqrt{n_2^{\mathrm{max}} + n_2^{\mathrm{min}}}$. We plot SNR as a function of the initial velocity v_{y0} in Fig. 4(a) and as a function of the pump strength η_1 in Fig. 4(b). The key feature which we observe is that SNR is high for high y_a^{pp} but, for low y_a^{pp}, the SNR can be below 1. To understand how the SNR R_{SN} can be improved, we use Eq. (10) to approximate the SNR in two limits. For $y_a^{\mathrm{pp}} \ll w_0$, we can perform Taylor expansion around $y_a = 0$ and obtain

$$R_{\mathrm{SN}} = \sqrt{\frac{n_2^{\mathrm{max}}}{2}} \left(\frac{y_a^{\mathrm{pp}}}{w_0} \right)^2 \tag{11}$$

to distinguish the maximum and minimum photon numbers, which is plotted as a magenta dotted curve in Figs. 4(a) and 4(b) and agrees with the numerically obtained SNR in the small-amplitude regimes which appear at small initial velocities and large pump strengths. For $y_a^{\mathrm{pp}} \gg w_0$, $n_2^{\mathrm{min}} \approx 0$, and thus, $R_{\mathrm{SN}} = \sqrt{n_2^{\mathrm{max}}}$, which is plotted in Figs. 4(a) and 4(b) as a yellow dash-dotted curve and agrees with the numerically obtained SNR for large-amplitude regimes. From these results, we see that the SNR can be improved by increasing n_2^{max} while keeping y_a^{pp} constant, which can be done by tuning other parameters as shown in Eq. (10).

VI. CAVITY-FEEDBACK-INDUCED BREAKDOWN OF SNAKE-STATE TRAJECTORIES

We now discuss two different effects on the snake-state trajectories which arise from strong atom-cavity coupling g_0. From Eqs. (8) and (10), we note that $\alpha_1 \propto \eta_1$ and $\alpha_2 \propto \eta_1 g_0^2$ (for $\eta_2 = 0$), and this distinction allows us to tune the relative number of photons in the two cavity modes. This is illustrated in Figs. 5(a), 5(c), and 5(e), where $\langle n_1 \rangle$ is much larger (smaller) than $\langle n_2 \rangle$ when g_0 is much smaller (larger) than g_{0c}. Here, $g_{0c} \simeq \sqrt{|\Delta_a||\Delta_c|/2}$ is obtained by setting $|\alpha_1| = |\alpha_2|$ in Eq. (8) and assuming $y_a = 0 = x_a$. Such a control on the sign of $n_1 - n_2$ allows us to tune the sign of the induced magnetic field gradient and thus the directionality of the generated snake-state trajectories [see Figs. 5(f) and 5(h); the same starting conditions, $x_{a0} = 0 = y_{a0}$ for $t = 0$, are used in both cases]. In Fig. 5(b), we show the corresponding behavior of $\langle v_x \rangle$, which is negative (positive) for $g_0 \ll (\gg)\ g_{0c}$.

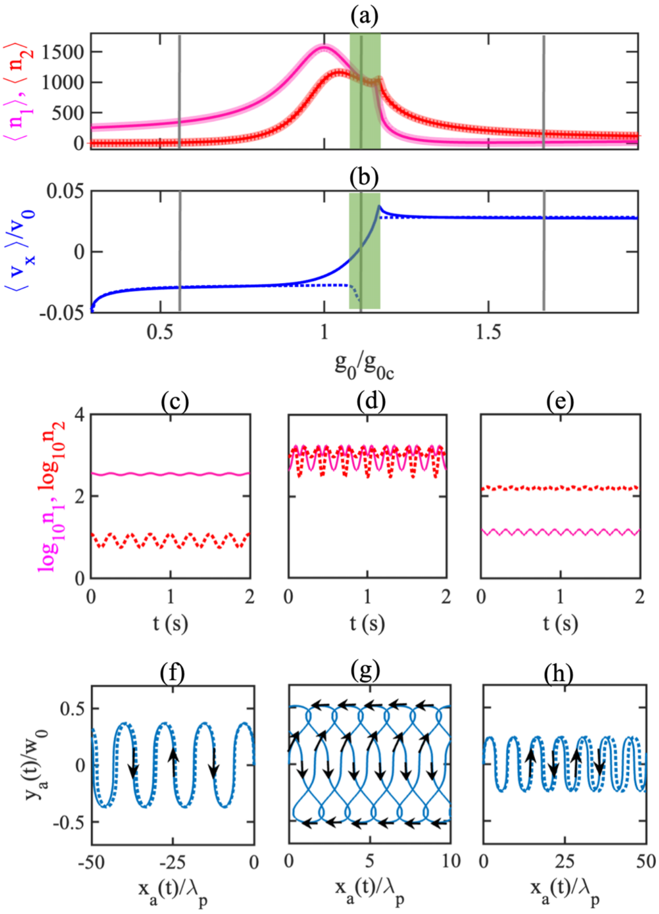

FIG. 5. (a) Average photon number variation in cavity modes 1 (magenta curve with dashes) and 2 (red curve with pluses) as a function of g_0. The shaded region denotes the corresponding peak-to-peak amplitude around the average photon number. The vertical gray solid lines correspond to $g_0 = (0.55, 1.1, 1.6)g_{0c}$ and represent the parameters used for plotting (c) and (f), (d) and (g), and (e) and (h), respectively. (b) Average drift velocity $\langle v_x \rangle$ (blue solid curve) is plotted as a function of the coupling strength g_0, which is normalized by $g_{0c} = 2\pi \times 90$ MHz (see text). The dotted blue curve shows the average drift speed in the absence of cavity feedback. The green vertical shaded region in (a) and (b) marks the region where the snake-state trajectory is destroyed due to dynamical cavity feedback. (c)–(e) The evolution of the photon numbers in cavity mode 1, n_1 (magenta solid curves), and mode 2, n_2 (red dotted curves), with time t and (f)–(h) the corresponding particle trajectories (solid curves) in the x-y plane for $g_0 = (0.55, 1.1, 1.6)g_{0c}$, respectively. The dotted trajectories in (f)–(h) depict the particle trajectories without cavity back-action, and the black arrows indicate the direction of increasing time in the time evolution. For all the calculations here, $\eta_1 = 80\kappa$, $\eta_2 = 0$, $v_{x0} = 0$, and $v_{y0} = 0.06v_0$ are considered, which give $g_0 = 0.29g_{0c}$ as the minimum coupling parameter required to get a trapped atomic trajectory.

The situation around $g_0 \approx g_{0c}$ [green vertical shaded regions in Figs. 5(a) and 5(b)] is more complicated because the dynamical cavity feedback leads to the breakdown of the snake-state trajectories. In this regime, the particle is still trapped near the cavity axis, but the resultant trajectory has a different topology than the snake states; see Fig. 5(g) for an example of such a trajectory. The origin of such complicated trajectories can be understood by looking at the corresponding time evolution of n_1 and n_2; see Fig. 5(d), where we note that the sign of $(n_1 - n_2)$ and hence the generated magnetic field gradient change amplitude and sign with time. The shaded region around the $\langle n_{1(2)}\rangle$ curves in Fig. 5(a) shows the peak-to-peak deviations from the mean value, and we find that the breakdown regime overlaps well with the region where the shaded regions of $\langle n_1\rangle$ and $\langle n_2\rangle$ overlap [see Fig. 5(d)]. To illustrate that such a breakdown happens due to cavity feedback, we additionally plot $\langle v_x\rangle$ [dotted blue line in Fig. 5(b)] and atomic trajectories [dotted trajectories in Figs. 5(f) and 5(h) and in Fig. 13 in Appendix D 3] for the case without feedback by fixing the photon number to the time-averaged values of the feedback case. For $|\langle n_1\rangle - \langle n_2\rangle| \gg 0$, the resultant snake-state trajectories in the two cases are very comparable [see the discussion related to Fig. 1(d) as well]. For $|\langle n_1\rangle - \langle n_2\rangle| \approx 0$, the atom is not trapped, which appears as a gap in the dotted curve in Fig. 5(b). We finally note that a similar breakdown of snake-state trajectories can be achieved by pumping both the cavity modes such that $\eta_1 \approx \eta_2$, which leads to comparable photon numbers in the two cavity modes.

VII. CONCLUSIONS AND OUTLOOK

This work focused on realizing the atomic analog of electronic snake-state trajectories in a ring cavity coupled to a single two-level atom. We showed that atom-cavity interaction in such a setup creates an effective spatially varying magnetic field with its strength depending on the difference in the photon numbers in the two counterpropagating running-wave cavity modes, which cannot be achieved in a standing-wave cavity. An atom in such a nonuniform perpendicular magnetic field follows snake-state trajectories and can be detected by monitoring the output cavity fields because they dynamically depend on the atom's position. The atomic snake-state trajectories provide an advantage over their electronic counterparts found in condensed-matter systems, where the charge carriers interact strongly with the system, making their manipulation difficult. The cold-atom surroundings allow us to engineer the properties of atomic snake states by changing the system parameters, such as the initial velocity of the atom, external pump strength, and atom-cavity coupling strength. We can also tune the effect of cavity back-action via atom-cavity coupling strength to change the topology of the snake states and create even richer dynamics.

Our proposed setup and methodology can be straightforwardly extended to induce magnetic fields with more intricate spatial structure by using multimode cavities [41] and can be used to detect the resulting topological trajectories via the output cavity fields. As a further extension of this work, one could study the behavior of a Bose-Einstein condensate in the presence of such a gauge field, where the interplay of atom-atom interactions, atom-cavity interaction, and cavity feedback can give rise to exotic topological phases of matter [101–103] and nonlinear instabilities [104,105]. It would also be exciting to study how such dynamical magnetic-field-induced snake states compete with other well-known phenomena in high-finesse ring cavities like superradiant Rayleigh scattering and collective recoil lasing [55,56,106]. Finally, we would also like to point out that determining whether such snake states have distinct topological features like the edge states in conventional quantum Hall systems in solid-state devices would require a lattice-based calculation, which is not within the scope of the current paper and may be carried out in the future.

ACKNOWLEDGMENTS

We thank M. Landini, F. Mivehvar, B. Prasanna Venkatesh, M. Bhattacharya, and P. Mondal for a number of helpful discussions at various stages of this work. S.G. thanks the ETH group of T. Esslinger and P. Öhberg at Heriot-Watt University for helpful discussions during his visits there. This work is supported by Board of Research in Nuclear Science (BRNS) [Department of Atomic Energy (DAE), Government of India] Grant No. 21/07/2015-BRNS/35041 (DAE SRC Outstanding Investigator scheme). P.S. was also supported by a UGC (Government of India) fellowship at the initial stage of this work.

APPENDIX A: DERIVATION OF THE SYSTEM HAMILTONIAN

In this Appendix, we derive the system Hamiltonian given in Eq. (1) of the main text. The single-particle Hamiltonian describing the coupled atom-cavity system is $\hat{H}_{\text{SP}} = \hat{H}_A + \hat{H}_C + \hat{H}_{A-C}$, where the atomic and cavity parts of the Hamiltonian are, respectively, given as

$$\hat{H}_A = \frac{\vec{P}^2}{2m_a}\hat{\mathbb{I}} + \frac{\hbar\omega_a\hat{\sigma}_z}{2}, \tag{A1}$$

$$\hat{H}_C = \hbar\omega_c(\hat{a}_1^\dagger\hat{a}_1 + \hat{a}_2^\dagger\hat{a}_2) + \hbar\eta_1(\hat{a}_1 e^{i\omega_p t} + \hat{a}_1^\dagger e^{-i\omega_p t}) + \hbar\eta_2(\hat{a}_2 e^{i\omega_p t} + \hat{a}_2^\dagger e^{-i\omega_p t}). \tag{A2}$$

Here, $E_e - E_g = \hbar\omega_a$. The single two-level excited atom scatters the photons into the two cavity modes. The atom-cavity interaction is given as

$$\hat{H}_{\text{int}} = \hat{H}_{A-C} = -\vec{d}\cdot\vec{E}_C, \tag{A3}$$

where $\vec{d} = d(\hat{\sigma}^+ + \hat{\sigma}^-)$ is the dipole operator, with $\hat{\sigma}^+ = |e\rangle\langle g|$ and $\hat{\sigma}^- = |g\rangle\langle e|$. $\hat{H}_{A-C}$ describes the interaction between the atom and the cavity fields (polarized along the y and z directions) in one arm of the ring cavity, and its corresponding electric field is given by

$$\vec{E}_C(\vec{r}) = \hat{e}_y\sqrt{\frac{\hbar\omega_c}{2\epsilon_0 V}}e^{-y^2/w_0^2}(\hat{a}_1 e^{ikx} + \hat{a}_1^\dagger e^{-ikx}) + \hat{e}_z\sqrt{\frac{\hbar\omega_c}{2\epsilon_0 V}}e^{-y^2/w_0^2}(\hat{a}_2 e^{-ikx} + \hat{a}_2^\dagger e^{ikx}). \tag{A4}$$

Here, ϵ_0 is the vacuum permittivity, and V is the mode volume. To get a clearer picture, we move to the interaction picture. The atomic field operators are given as $\hat{\sigma}^\pm(t) = \hat{\sigma}^\pm(0)e^{\pm i\omega_a t}$.

The time evolution of the cavity-field operators is written as $\hat{a}_{1(2)}(t) = \hat{a}_{1(2)}(0)e^{-i\omega_c t}$. Similarly, for $\hat{a}^\dagger_{1,2}$, we get $\hat{a}^\dagger_{1,2}(t) = \hat{a}^\dagger_{1,2}(0)e^{i\omega_c t}$. Using (A4), the atom-cavity-field interaction in the interaction picture takes the following form:

$$\begin{aligned}\hat{H}^I_{A-C} &= -\vec{d}\cdot\vec{E}_C\\ &= \hbar g_1(y)[\hat\sigma^+(t)\hat a_1(t)e^{ikx} + \hat\sigma^-(t)\hat a_1(t)e^{ikx}\\ &\quad + \hat\sigma^+(t)\hat a_1^\dagger(t)e^{-ikx} + \hat\sigma^-(t)\hat a_1^\dagger(t)e^{ikx}]\\ &\quad + \hbar g_2(y)[\hat\sigma^+(t)\hat a_2(t)e^{-ikx} + \hat\sigma^-(t)\hat a_2(t)e^{-ikx}\\ &\quad + \hat\sigma^+(t)\hat a_2^\dagger(t)e^{ikx} + \hat\sigma^-(t)\hat a_2^\dagger(t)e^{ikx}]. \end{aligned} \tag{A5}$$

If $\omega_a \sim \omega_c$, then the terms with $e^{\pm i(\omega_a-\omega_c)t}$ will have small transition amplitudes that are proportional to $\frac{1}{(\omega_a+\omega_c)^2}$. Therefore, the fast oscillating terms with frequency $\omega_a+\omega_c$ can be neglected compared to the slow oscillating terms with frequency $\omega_a-\omega_c$. Transforming back to the Schrödinger picture, we get [107–109]

$$\begin{aligned}\hat{H}_{A-C} &= \hbar g_1(y)[\hat\sigma^+\hat a_1 e^{ikx} + \hat\sigma^-\hat a_1^\dagger e^{-ikx}]\\ &\quad + \hbar g_2(y)[\hat\sigma^+\hat a_2 e^{-ikx} + \hat\sigma^-\hat a_2^\dagger e^{ikx}].\end{aligned}$$

The transformation to the rotating frame of the pump field is carried through the unitary operator,

$$\hat U(t) = e^{-i\omega_p t(\frac{\hat\sigma_z}{2}+\hat a_1^\dagger\hat a_1+\hat a_2^\dagger\hat a_2)}.$$

Since the observables and the states respectively transform as $\hat O_{\mathrm{RF}} = \hat U^\dagger\hat O\hat U$ and $|\Psi_{\mathrm{RF}}\rangle = \hat U^\dagger|\Psi\rangle$ in the rotating frame, the Schrödinger equation transforms as

$$i\hbar\frac{\partial}{\partial t}|\Psi_{\mathrm{RF}}\rangle = i\hbar\left[\frac{\partial}{\partial t}(\hat U^\dagger|\Psi\rangle)\right] = \hat H_{\mathrm{RF}}|\Psi_{\mathrm{RF}}\rangle,$$

where

$$\hat H_{\mathrm{RF}} = \frac{-\hbar\omega_p\hat\sigma_z}{2} - \hbar\omega_p\hat a_1^\dagger\hat a_1 - \hbar\omega_p\hat a_2^\dagger\hat a_2 + \hat U^\dagger\hat H_{\mathrm{SP}}\hat U \tag{A6}$$

is the single-particle Hamiltonian in the rotating frame of the pump field. To get $\hat U^\dagger\hat H_{\mathrm{SP}}\hat U$, we use the Baker-Hausdorff formula, which finally gives us

$$\begin{aligned}\hat H_{\mathrm{RF}} &= \frac{\hat P^2}{2m_a}\mathbb{I} - \frac{\hbar\Delta_a\hat\sigma_z}{2} - \hbar\Delta_c(\hat a_1^\dagger\hat a_1 + \hat a_2^\dagger\hat a_2)\\ &\quad + \hbar\eta_1(\hat a_1^\dagger + \hat a_1) + \hbar\eta_2(\hat a_2^\dagger + \hat a_2)\\ &\quad + \hbar g_1(y)[\hat\sigma^+\hat a_1 e^{ikx} + \hat\sigma^-\hat a_1^\dagger e^{-ikx}]\\ &\quad + \hbar g_2(y)[\hat\sigma^+\hat a_2 e^{-ikx} + \hat\sigma^-\hat a_2^\dagger e^{ikx}],\end{aligned} \tag{A7}$$

where $\Delta_a = \omega_p - \omega_a$ is the atom-pump detuning and $\Delta_c = \omega_p - \omega_c$ is the cavity-pump detuning. This is the system Hamiltonian considered in Eq. (1) of the main text.

The interaction Hamiltonian $\hat H_I$ in the bare-state basis contains off-diagonal terms and can be written as

$$\hat H_I = \begin{bmatrix} -\frac{\hbar}{2}\Delta_a + C_t & \hbar c_1\\ \hbar c_1^* & \frac{\hbar}{2}\Delta_a + C_t\end{bmatrix},$$

where we have used $C_t = -\hbar\Delta_c(|\alpha_1|^2 + |\alpha_2|^2) + 2\hbar\eta_1|\alpha_1|\cos\phi_1 + 2\hbar\eta_2|\alpha_2|\cos\phi_2$ and $c_1 = g(y)\alpha_1 e^{ikx} + g(y)\alpha_2 e^{-ikx}$.

We diagonalize the Hamiltonian $\hat H_I$ in the space spanned by the atom-photon bare states, namely, $|e,\alpha_1,\alpha_2\rangle$ and $|g,\alpha_1,\alpha_2\rangle$, and obtain the following eigenstates, referred to as dressed states $|D_1\rangle$ and $|D_2\rangle$, for the coupled atom-photon system, with E_1 and E_2 being their eigenvalues, respectively:

$$\begin{aligned}E_1 &= -\hbar\Delta_c(|\alpha_1|^2 + |\alpha_2|^2) + 2\hbar\eta_1|\alpha_1|\cos\phi_1\\ &\quad + 2\hbar\eta_2|\alpha_2|\cos\phi_2 - \frac{\hbar G}{2},\end{aligned} \tag{A8a}$$

$$|D_1\rangle = \frac{1}{\sqrt{2G(G+\Delta_a)}}\begin{bmatrix} G+\Delta_a\\ -2c_1^*\end{bmatrix}, \tag{A8b}$$

$$\begin{aligned}E_2 &= -\hbar\Delta_c(|\alpha_1|^2 + |\alpha_2|^2) + 2\hbar\eta_1|\alpha_1|\cos\phi_1\\ &\quad + 2\hbar\eta_2|\alpha_2|\cos\phi_2 + \frac{\hbar G}{2},\end{aligned} \tag{A8c}$$

$$|D_2\rangle = \frac{1}{\sqrt{2G(G+\Delta_a)}}\begin{bmatrix} 2c_1\\ G+\Delta_a\end{bmatrix}, \tag{A8d}$$

where$|c_1|^2 = [g^2(y)|\alpha_1|^2 + g^2(y)|\alpha_2|^2]$ and $G = \sqrt{\Delta_a^2 + 4|c_1|^2}$.

Now, we derive the equation of motion for the probability amplitude ψ_1 to find the atom in the lowest-energy dressed state $|D_1\rangle$. In the dressed-state basis ($|D_j\rangle$ basis) for the internal Hilbert space of the atom at any point $\vec r$, the full state vector of the atom and the corresponding equation of motion are [1]

$$|\Psi(\vec r,t)\rangle = \sum_{j=1,2}\psi_j(\vec r,t)|D_j\rangle, \tag{A9}$$

$$i\hbar\frac{\partial}{\partial t}|\Psi(\vec r,t)\rangle = \hat H_{\mathrm{RF}}|\Psi(\vec r,t)\rangle. \tag{A10}$$

The action of the momentum operator $\hat P$ on the atomic wave function $|\Psi(\vec r,t)\rangle$ is given as [1]

$$\begin{aligned}\hat P|\Psi(\vec r,t)\rangle &= -i\hbar\vec\nabla\left[\sum_{j=1,2}\psi_j(\vec r,t)|D_j\rangle\right]\\ &= -i\hbar\sum_j\{[\vec\nabla\psi_j(\vec r,t)]|D_j\rangle + \psi_j(\vec r,t)(\vec\nabla|D_j\rangle)\}\\ &= \sum_{j,l=1,2}[\vec p\delta_{l,j} - \vec{\mathbf{A}}_{l,j}]\psi_j|D_l\rangle,\end{aligned} \tag{A11}$$

where $\vec{\mathbf{A}}_{l,j} = i\hbar\langle D_l|\vec\nabla|D_j\rangle$ is the vector potential and $\vec p = -i\hbar\vec\nabla$ does not act on the spinorial part. From this, we can straightforwardly write the kinetic-energy term as

$$\begin{aligned}\frac{\hat P^2}{2m_a}|\Psi(\vec r,t)\rangle &= \frac{1}{2m_a}\sum_{j,l,m=1,2}\{(\vec p\delta_{l,j} - \vec{\mathbf{A}}_{l,j})\\ &\quad\times[(\vec p\delta_{m,l} - \vec{\mathbf{A}}_{m,l})\psi_j]\}|D_m\rangle.\end{aligned} \tag{A12}$$

We can write down a 2×2 matrix $\vec{\mathbf{A}}$ whose components are given as $\vec{\mathbf{A}}_{l,j} = i\hbar\langle D_l|\vec\nabla|D_j\rangle$. We project the Schrödinger equation (A10) to the lowest-energy dressed state $|D_1\rangle$ to obtain Eq. (2) of the main text.

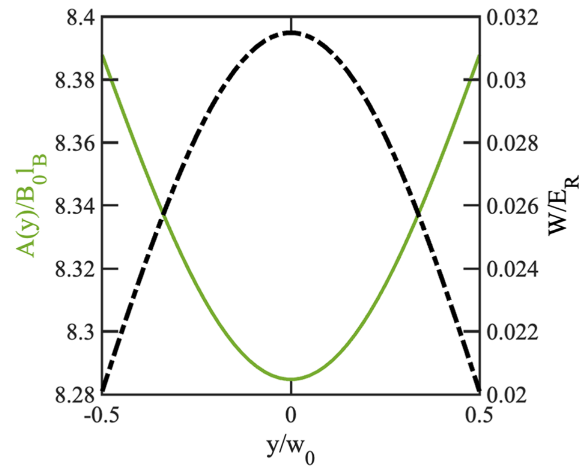

FIG. 6. Comparison of scalar potential W (black dash-dotted curve) and vector potential A (green solid curve).

APPENDIX B

1. Effect of the scalar potential W on the magnetic field $\vec{B}$

We provide a comparison of the vector and the scalar potentials in Fig. 6 which shows that the scalar potential makes a negligible contribution to the system dynamics. We can switch to a multilevel description which allows for the possibility of magic wavelengths for which the effect of the scalar potential can be canceled.

2. Effect of an additional trapping potential on the magnetic field $\vec{B}$

The off-diagonal terms of the interaction Hamiltonian $\hat{H}_I$ which couple the bare states of the atom-cavity system are mainly responsible for the shape and emergence of a magnetic field. An external harmonic trapping potential provides only an additional confining potential apart from the dressed-state energy E_1 in Eq. (2) of the main text. For a harmonic trap with a frequency of $\Omega_0 \approx 2\pi \times 50$ Hz, the typical length scales are approximately 4 μm. However, for the parameters considered in this work, the length scales associated with snake trajectories are of the order of $\approx$9 μm and hence would make the detection of the snake states difficult. Therefore, instead of a harmonic trap we can use a free atomic beam which is not trapped in the x-y plane and thus does not restrict the length scale of the trajectory, making their detection possible.

APPENDIX C

1. Reconstruction of the atomic trajectory from output cavity fields

We use the output from cavity mode 2 to recreate the snake-state trajectory of the atom using the approximations considered in Sec. IV. The x position of the atom can be estimated by the phase $\phi_{2,\mathrm{ss}}$, given as $\frac{x_{a,\mathrm{cav}}}{\lambda_p} = \frac{\phi_{2,\mathrm{ss}}}{2k\lambda_p}$, and the y position of the atom can be estimated from the values of n_2, given by the approximated formula

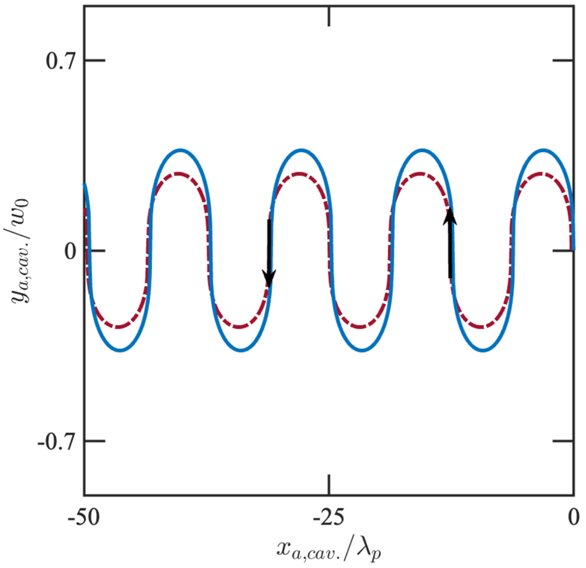

FIG. 7. The solid blue line shows the snake-state trajectory, and the maroon dash-dotted line shows the reconstructed snake-state trajectory using parameters of the output cavity field α_2. Refer to the text for details.

$$\frac{y_{a,\mathrm{cav}}}{w_0} = \frac{1}{2}\sqrt{\log_{10}\left(\frac{n_2^{\max}}{n_2}\right)}, \tag{C1}$$

where we have inverted the formula for $|\alpha_2|$ given in Eq. (10) and have used $\frac{\eta_1^2 g_0^4}{\Delta_a^2(\tilde{\Delta}_c^2+\tilde{\kappa}^2)^2} \simeq n_2^{\max}$ (keeping $y = 0$). Experimentally, we can measure $n_2^{\max}$ directly, so the y reconstruction will be closer to the actual trajectory. With these formulas, we reconstruct the snake-state trajectory in Fig. 7. We also invert the sign of the reconstructed y_a when it reaches zero because n_2 does not carry this information explicitly. A variation in the peak-to-peak values of $y_{a,\mathrm{cav}}$ arises due to the approximations considered.

2. Photon numbers in mode 1 and their phase ϕ_1

We provide the plots for the photon numbers in mode 1 and their Fourier transforms, which shows a peak at $2\nu_0$, in Figs. 8(a) and 8(b). The peaks at $4\nu_0$ and $6\nu_0$ are not visible here, but their amplitude increases for higher initial speeds along the y direction. Phase ϕ_1 of photons in mode 1 [see Fig. 8(c)] shows a small oscillation amplitude which arises from the y_a dependence of U and γ. The Fourier transform of $e^{i\phi_1}$ shows a small amplitude peak at $2\nu_0$ [see Fig. 8(d)] which is different from the Fourier transform of $e^{i\phi_{2,\mathrm{ss}}}$ because there is no x_a dependence in ϕ_1.

3. Effect of the Doppler shift on the atomic trajectory

The motion of the atom with respect to the propagation direction of the cavity field could give rise to a Doppler shift. The Doppler shift is given by $\vec{k} \cdot \vec{v}$, where $\vec{k}$ is the wave vector of the cavity field ($\vec{k} = k\hat{x}$ for cavity mode $\hat{a}_1$ and $\vec{k} = -k\hat{x}$ is for cavity mode $\hat{a}_2$) and $\vec{v}$ is the velocity of the atom. The modified steady-state expression for the two cavity fields after

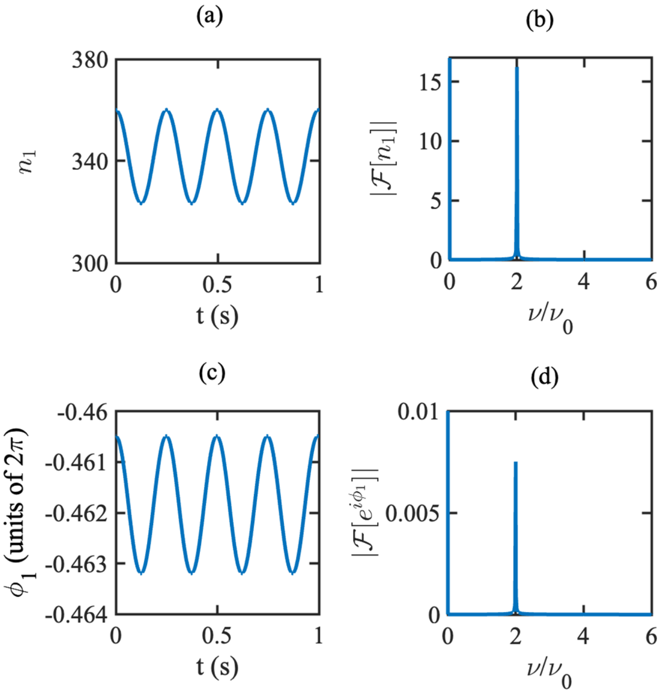

FIG. 8. (a) Photon numbers in cavity mode 1 n_1 as a function of time t. (b) Fourier transform of n_1, which shows a peak at $2\nu_0$. (c) Phase ϕ_1 of photons in mode 1 as a function of time t. (d) Fourier transform of $e^{i\phi_1}$, which also shows a peak at $2\nu_0$.

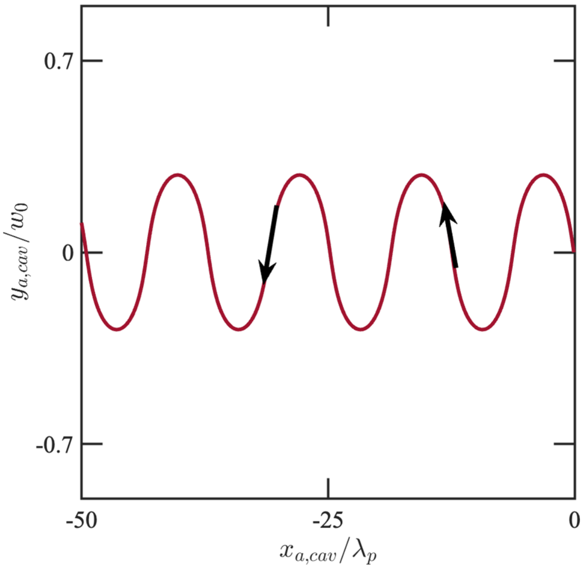

FIG. 9. The reconstructed snake-state trajectory including the effect of the Doppler shift.

including the effect of the Doppler shift is given as

$$\alpha_{1(2)} = \langle \hat{a}_{1(2)} \rangle = \langle D_1 | \hat{a}_{1(2)} | D_1 \rangle = \frac{i\eta_{1(2)}(i\bar{\Delta}_c - \bar{\kappa}) + i\eta_{2(1)}(iU + \gamma)e^{\mp 2ikx_a(t) + 2i\vec{k}\cdot\vec{v}t}}{(i\bar{\Delta}_c - \bar{\kappa})^2 - (iU + \gamma)^2}. \tag{C2}$$

Solving Eqs. (7a) and (7b) simultaneously with Eq. (C2) (assuming initial conditions similar to those used in Sec. III), we observe in Fig. 9 that the resulting snake-state trajectories do not show any effect of the Doppler shift. This is because the Doppler shifts for the two counterpropagating fields are opposite and hence have no effect on the resulting atomic trajectories. However, the time variation of phase ϕ_2 is now given as

$$\phi_2 \approx \phi_{2,\mathrm{ss}} + \phi_{2,\mathrm{ds}} = 2kx_a(t) + 2\vec{k}\cdot\vec{v}t \tag{C3}$$

and is shown in Fig. 10. An increase in the oscillation amplitude of ϕ_2 arises due to the time dependence of the Doppler shift component ($\phi_{2,\mathrm{ds}} \approx 2\vec{k}\cdot\vec{v}t$) in the phase. The wave vector for cavity mode 2 is $-k\hat{x}$, and the atom moves along the $-x$ direction, which allows us to write

$$\phi_2 = 2kx_a(t) + 2kt\frac{dx_a}{dt}$$
$$\Rightarrow \frac{dx_a}{dt} = -\frac{x_a}{t} + \frac{\phi_2}{2kt}. \tag{C4}$$

We solve the above differential equation numerically to obtain $x_{a,cav}$, and we use $y_{a,cav}$ from Eq. (C1) to reconstruct the snake-state trajectory of the atom in Fig. 9 from the cavity 2 output. A variation in the peak-to-peak values of $y_{a,cav}$ arises due to the approximations considered.

APPENDIX D

1. Snake-state trajectories for different initial conditions

We look at the structure of snake-state trajectories for different initial speeds v_{y0} along the y direction. We consider $\eta_1 = 80\kappa, \eta_2 = 0, x_0 = 0 = y_0$, and $v_{x0} = 0$. We plot the peak frequency ν_0 of the Fourier transform of y_a in Fig. 11(a) and observe two different regimes. Up to $v_{y0} \approx 0.13v_0$, ν_0 increases. In this regime, the oscillation amplitude

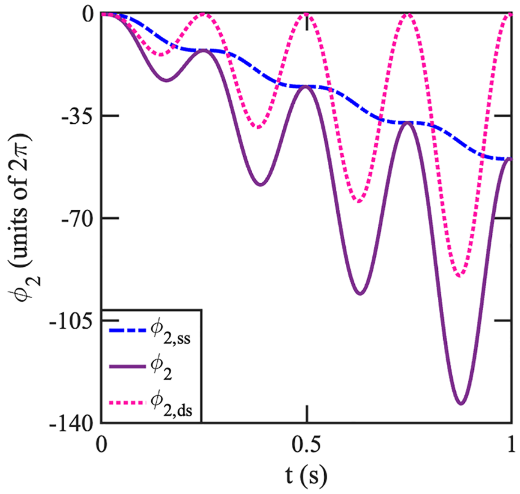

FIG. 10. Full phase ϕ_2 (purple solid curve) of cavity mode 2 as a function of time t, showing the contributions of $\phi_{2,\mathrm{ss}}$ (blue dash-dotted curve) and $\phi_{2,ds}$ (magenta dotted curve), including the effect of the Doppler shift.

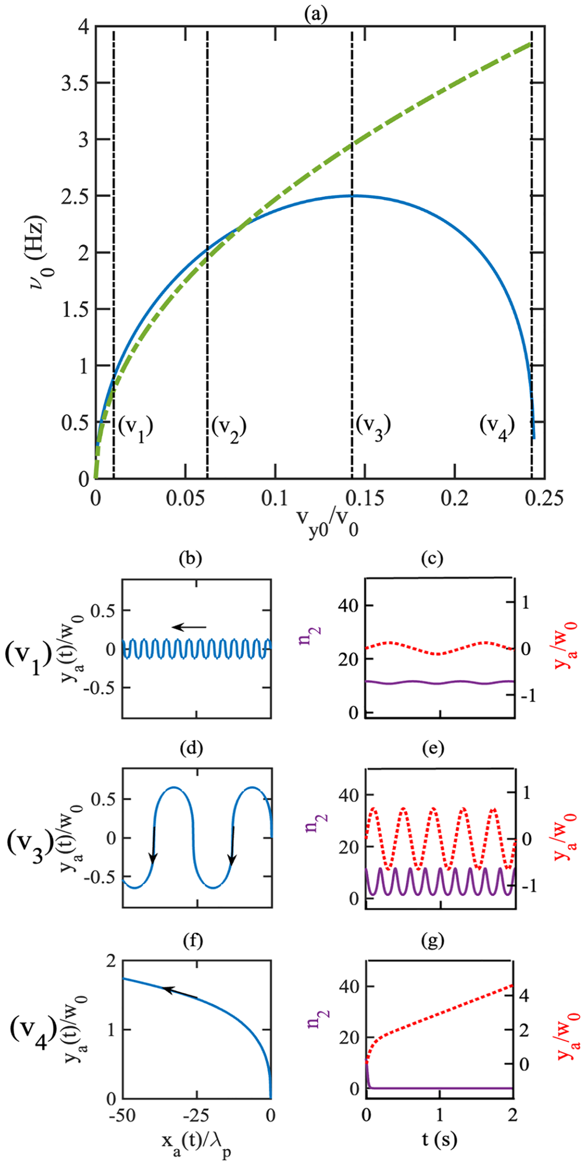

FIG. 11. (a) Oscillation frequency ν_0 (blue solid curve) of atomic position y_a along the y direction plotted as a function of initial velocity v_{y0} along the y direction for fixed $v_{x0} = 0$. The green dash-dotted curve shows the analytical frequency obtained from the $y_{\rm period}$ formula in Eq. (9). We consider four points, (v_1), (v_2), (v_3), and (v_4), of the initial velocity and show the corresponding trajectories and photon numbers. The v_{y0} velocity at point (v_2) was considered in the main text, and therefore, its trajectories are not shown here. Snake-state trajectories for $v_{y0} = v_1$, v_3, and v_4 are shown in (b), (d), and (f), respectively. Correspondingly, the photon number (purple solid curve) in mode 2 (left y axis) and y_a/w_0 (red dotted curve) variation (right y axis) as a function of time are shown in (c), (e), and (g). For parameters and explanation, refer to the text.

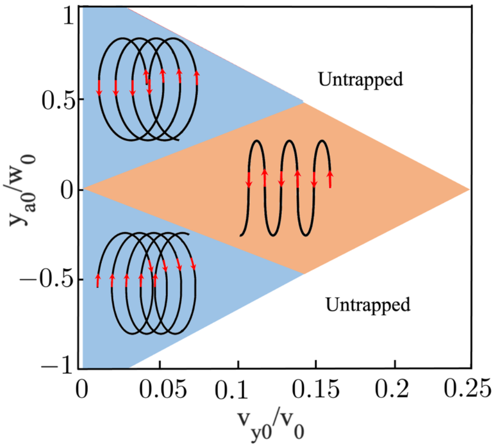

FIG. 12. Phase diagram for the atomic trajectories (blue shaded regions); the particle follows cyclotron orbits (orange shaded region), the particle follows snake-state trajectories, and the white region indicates the regime where the atom is not trapped by the synthetic magnetic field. y_{a0} and v_{y0} are the initial position and speed of the atom along the y direction, respectively. w_0 is the waist of the cavity mode, and v_0 is a natural scale of the particle speed (see text). The red arrows indicate the direction of particle evolution with increasing time.

along the y direction increases with increasing v_{y0} due to the increased initial speed, and the amplitude of n_2 increases correspondingly, as shown in Figs. 11(c) and 11(e). The spatial period along the x direction also increases, as shown in Figs. 11(b) and 11(d). The green dash-dotted curve in Fig. 11(a) also shows that the analytical frequency obtained from the $y_{\rm period}$ formula in Eq. (9) fits better for small initial velocities v_{y0}.

For initial velocities higher than $0.13v_0$, ν_0 decreases, and the amplitude of the snake-state trajectories along the y direction increases. For $v_{y0} > 0.24v_0$, the atom cannot be trapped along the y direction by the synthetic magnetic field [see Fig. 11(f)], and the corresponding photon number n_2 decays to zero [see Fig. 11(g)].

2. Phase diagram of the atomic trajectories

The atom subjected to the perpendicular nonuniform artificial magnetic field can follow snake-state trajectories or normal orbits depending on the initial velocity and initial position along the y axis. We provide a qualitative phase diagram to visualize the various regimes in Fig. 12 for $g_0 = 0.55g_{0c}$, $\eta_1 = 80\kappa$, and $\eta_2 = 0$. When the atom is far away ($|y_a| > 0.5w_0$) from the cavity center, it sees a nearly uniform magnetic field with a small slope [see Fig. 1(b)] and performs cyclotron orbits (blue shaded region) for small v_{y0} values. For high v_{y0} values, the uniform magnetic field is not strong enough to keep the atom trapped, and therefore, it escapes the cavity. We obtain clockwise (counterclockwise) normal orbits for $y_{a0} < (>)\ 0$. When the atom starts near the cavity center ($x_{a0} = 0$ and $|y_a| < 0.5w_0$), it follows normal orbits for very small v_{y0}. An increase in v_{y0} increases the range of y_{a0} where the atom follows snake-state trajectories (orange shaded region) for $v_{y0} > 0$ as it sees a spatially varying magnetic field which reverses sign along the $y = 0$ axis. For $0.13v_0 < v_{y0} < 0.24v_0$, the range of y_{a0} where the snake-state motion is allowed decreases. The atom escapes the cavity for $v_{y0} > 0.24v_0$. Changing η_1 gives a similar phase diagram with an increase in the value of the escape velocity for increasing η_1.

3. Atomic trajectories in the breakdown regime

We plot the atomic trajectories in the breakdown regime for coupling strength $g_0 = 1.1g_{0c}$ with and without considering the cavity feedback in Fig. 13. The absence of feedback results in a left-moving snakelike trajectory as opposed to the case in which we consider the effect of cavity feedback on the atomic trajectory, which results in a complicated right-moving trajectory.

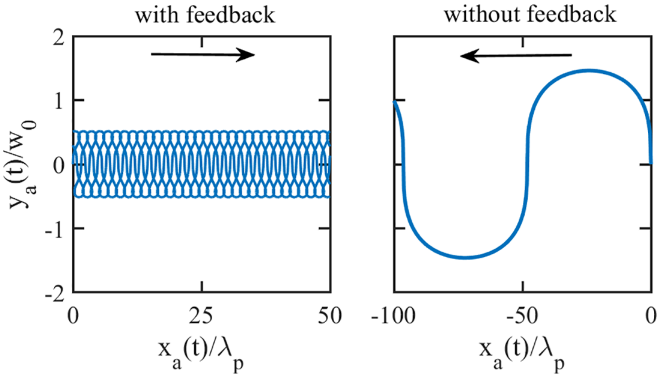

FIG. 13. For $g_0 = 1.1g_{0c}$, we show the trajectories of the atom with and without feedback ($\langle n_1 \rangle = 946$ and $\langle n_2 \rangle = 894$). The initial velocity $v_{x0} = 0$, and $v_{y0} = 0.06v_0$.

[1] J. Dalibard, F. Gerbier, G. Juzeliūnas, and P. Öhberg, Colloquium: Artificial gauge potentials for neutral atoms, Rev. Mod. Phys. **83**, 1523 (2011).

[2] N. Goldman, G. Juzeliūnas, P. Öhberg, and I. B. Spielman, Light-induced gauge fields for ultracold atoms, Rep. Prog. Phys. **77**, 126401 (2014).

[3] I. B. Spielman, Raman processes and effective gauge potentials, Phys. Rev. A **79**, 063613 (2009).

[4] F. Gerbier and J. Dalibard, Gauge fields for ultracold atoms in optical superlattices, New J. Phys. **12**, 033007 (2010).

[5] D. Jaksch and P. Zoller, Creation of effective magnetic fields in optical lattices: The Hofstadter butterfly for cold neutral atoms, New J. Phys. **5**, 56 (2003).

[6] A. S. Sørensen, E. Demler, and M. D. Lukin, Fractional quantum Hall states of atoms in optical lattices, Phys. Rev. Lett. **94**, 086803 (2005).

[7] A. R. Kolovsky, Creating artificial magnetic fields for cold atoms by photon-assisted tunneling, Europhys. Lett. **93**, 20003 (2011).

[8] N. R. Cooper, Optical flux lattices for ultracold atomic gases, Phys. Rev. Lett. **106**, 175301 (2011).

[9] J. Struck, C. Ölschläger, R. Le Targat, P. Soltan-Panahi, A. Eckardt, M. Lewenstein, P. Windpassinger, and K. Sengstock, Quantum simulation of frustrated classical magnetism in triangular optical lattices, Science **333**, 996 (2011).

[10] M. Aidelsburger, M. Atala, S. Nascimbène, S. Trotzky, Y.-A. Chen, and I. Bloch, Experimental realization of strong effective magnetic fields in an optical lattice, Phys. Rev. Lett. **107**, 255301 (2011).

[11] P. Hauke, O. Tieleman, A. Celi, C. Ölschläger, J. Simonet, J. Struck, M. Weinberg, P. Windpassinger, K. Sengstock, M. Lewenstein, and A. Eckardt, Non-Abelian gauge fields and topological insulators in shaken optical lattices, Phys. Rev. Lett. **109**, 145301 (2012).

[12] J. Struck, C. Ölschläger, M. Weinberg, P. Hauke, J. Simonet, A. Eckardt, M. Lewenstein, K. Sengstock, and P. Windpassinger, Tunable gauge potential for neutral and spinless particles in driven optical lattices, Phys. Rev. Lett. **108**, 225304 (2012).

[13] H. Miyake, G. A. Siviloglou, C. J. Kennedy, W. C. Burton, and W. Ketterle, Realizing the Harper Hamiltonian with laser-assisted tunneling in optical lattices, Phys. Rev. Lett. **111**, 185302 (2013).

[14] M. Aidelsburger, M. Atala, M. Lohse, J. T. Barreiro, B. Paredes, and I. Bloch, Realization of the Hofstadter Hamiltonian with ultracold atoms in optical lattices, Phys. Rev. Lett. **111**, 185301 (2013).

[15] Y.-J. Lin, R. L. Compton, A. R. Perry, W. D. Phillips, J. V. Porto, and I. B. Spielman, Bose-Einstein condensate in a uniform light-induced vector potential, Phys. Rev. Lett. **102**, 130401 (2009).

[16] Y.-J. Lin, R. L. Compton, K. Jimenez-Garcia, J. V. Porto, and I. B. Spielman, Synthetic magnetic fields for ultracold neutral atoms, Nature (London) **462**, 628 (2009).

[17] Y.-J. Lin, K. Jiménez-García, and I. B. Spielman, Spin–orbit-coupled Bose–Einstein condensates, Nature (London) **471**, 83 (2011).

[18] F. Mivehvar and D. L. Feder, Synthetic spin-orbit interactions and magnetic fields in ring-cavity QED, Phys. Rev. A **89**, 013803 (2014).

[19] I. Bloch, J. Dalibard, and W. Zwerger, Many-body physics with ultracold gases, Rev. Mod. Phys. **80**, 885 (2008).

[20] I. Buluta and F. Nori, Quantum simulators, Science **326**, 108 (2009).

[21] I. Bloch, Ultra cold quantum gases in optical lattices, Nat. Phys. **1**, 23 (2005).

[22] J. Schmiedmayer, Quantum wires and quantum dots for neutral atoms, Eur. Phys. J. D **4**, 57 (1998).

[23] N. R. Cooper, Rapidly rotating atomic gases, Adv. Phys. **57**, 539 (2008).

[24] S. Viefers, Quantum Hall physics in rotating Bose-Einstein condensates, J. Phys.: Condens. Matter **20**, 123202 (2008).

[25] A. L. Fetter, Rotating trapped Bose-Einstein condensates, Rev. Mod. Phys. **81**, 647 (2009).

[26] J. Ruhman, E. Berg, and E. Altman, Topological states in a one-dimensional Fermi gas with attractive interaction, Phys. Rev. Lett. **114**, 100401 (2015).

[27] L. Jiang, T. Kitagawa, J. Alicea, A. R. Akhmerov, D. Pekker, G. Refael, J. I. Cirac, E. Demler, M. D. Lukin, and P. Zoller, Majorana fermions in equilibrium and in driven cold-atom quantum wires, Phys. Rev. Lett. **106**, 220402 (2011).

[28] M. Aidelsburger, M. Lohse, C. Schweizer, M. Atala, J. T. Barreiro, S. Nascimbéne, N. R. Cooper, I. Bloch, and N. Goldman, Measuring the Chern number of Hofstadter bands with ultracold bosonic atoms, Nat. Phys. **11**, 162 (2015).

[29] G. Jotzu, M. Messer, R. Desbuquois, M. Lebrat, T. Uehlinger, D. Greif, and T. Esslinger, Experimental realization of the topological Haldane model with ultracold fermions, Nature (London) **515**, 237 (2014).

[30] E. Kapit and E. Mueller, Optical-lattice Hamiltonians for relativistic quantum electrodynamics, Phys. Rev. A **83**, 033625 (2011).

[31] D. Banerjee, M. Bögli, M. Dalmonte, E. Rico, P. Stebler, U. J. Wiese, and P. Zoller, Atomic quantum simulation of U(N) and SU(N) non-Abelian lattice gauge theories, Phys. Rev. Lett. **110**, 125303 (2013).

[32] U.-J. Wiese, Ultracold quantum gases and lattice systems: Quantum simulation of lattice gauge theories, Ann. Phys. (Berlin, Ger.) **525**, 777 (2013).

[33] D. Banerjee, M. Dalmonte, M. Müller, E. Rico, P. Stebler, U.-J. Wiese, and P. Zoller, Atomic quantum simulation of dynamical gauge fields coupled to fermionic matter: From string breaking to evolution after a quench, Phys. Rev. Lett. **109**, 175302 (2012).

[34] L. Tagliacozzo, A. Celi, P. Orland, M. W. Mitchell, and M. Lewenstein, Simulation of non-Abelian gauge theories with optical lattices, Nat. Commun. **4**, 2615 (2013).

[35] E. Zohar, J. I. Cirac, and B. Reznik, Cold-atom quantum simulator for SU(2) Yang-Mills lattice gauge theory, Phys. Rev. Lett. **110**, 125304 (2013).

[36] K. Baumann, C. Gulerin, F. Brennecke, and T. Esslinger, Dicke quantum phase transition with a superfluid gas in an optical cavity, Nature (London) **464**, 1301 (2010).

[37] P. Shakya, A. Ratnakar, and S. Ghosh, Dimensional cross-over in self-organised super-radiant phases of ultra-cold atoms inside a cavity, J. Phys. B **56**, 035301 (2023).

[38] J. Léonard, A. Morales, P. Zupancic, T. Esslinger, and T. Donner, Supersolid formation in a quantum gas breaking a continuous translational symmetry, Nature (London) **543**, 87 (2017).

[39] R. M. Kroeze, Y. Guo, and B. L. Lev, Dynamical spin-orbit coupling of a quantum gas, Phys. Rev. Lett. **123**, 160404 (2019).

[40] D. Dreon, A. Baumgärtner, X. Li, S. Hertlein, T. Esslinger, and T. Donner, Self-oscillating pump in a topological dissipative atom–cavity system, Nature (London) **608**, 494 (2022).

[41] K. E. Ballantine, B. Lev, and J. Keeling, Meissner-like effect for a synthetic gauge field in multimode cavity QED, Phys. Rev. Lett. **118**, 045302 (2017).

[42] B. Padhi and S. Ghosh, Spin-orbit-coupled Bose-Einstein condensates in a cavity: Route to magnetic phases through cavity transmission, Phys. Rev. A **90**, 023627 (2014).

[43] F. Mivehvar, H. Ritsch, and F. Piazza, Cavity-quantum-electrodynamical toolbox for quantum magnetism, Phys. Rev. Lett. **122**, 113603 (2019).

[44] J. Keeling, M. J. Bhaseen, and B. D. Simons, Fermionic superradiance in a transversely pumped optical cavity, Phys. Rev. Lett. **112**, 143002 (2014).

[45] F. Piazza and P. Strack, Umklapp superradiance with a collisionless quantum degenerate Fermi gas, Phys. Rev. Lett. **112**, 143003 (2014).

[46] Y. Chen, Z. Yu, and H. Zhai, Superradiance of degenerate Fermi gases in a cavity, Phys. Rev. Lett. **112**, 143004 (2014).

[47] J.-S. Pan, X.-J. Liu, W. Zhang, W. Yi, and G.-C. Guo, Topological superradiant states in a degenerate Fermi gas, Phys. Rev. Lett. **115**, 045303 (2015).

[48] Z. Zheng, X.-B. Zou, and G.-C. Guo, Synthetic topological Kondo insulator in a pumped optical cavity, New J. Phys. **20**, 023039 (2018).

[49] C. Kollath, A. Sheikhan, S. Wolff, and F. Brennecke, Ultracold fermions in a cavity-induced artificial magnetic field, Phys. Rev. Lett. **116**, 060401 (2016).

[50] A. Sheikhan, F. Brennecke, and C. Kollath, Cavity-induced chiral states of fermionic quantum gases, Phys. Rev. A **93**, 043609 (2016).

[51] S. Wolff, A. Sheikhan, and C. Kollath, Dissipative time evolution of a chiral state after a quantum quench, Phys. Rev. A **94**, 043609 (2016).

[52] A. Sheikhan, F. Brennecke, and C. Kollath, Cavity-induced generation of nontrivial topological states in a two-dimensional Fermi gas, Phys. Rev. A **94**, 061603(R) (2016).

[53] C.-M. Halati, A. Sheikhan, and C. Kollath, Cavity-induced artificial gauge field in a Bose-Hubbard ladder, Phys. Rev. A **96**, 063621 (2017).

[54] C.-M. Halati, A. Sheikhan, and C. Kollath, Cavity-induced spin-orbit coupling in an interacting bosonic wire, Phys. Rev. A **99**, 033604 (2019).

[55] H. Ritsch, P. Domokos, F. Brennecke, and T. Esslinger, Cold atoms in cavity-generated dynamical optical potentials, Rev. Mod. Phys. **85**, 553 (2013).

[56] F. Mivehvar, F. Piazza, T. Donner, and H. Ritsch, Cavity QED with quantum gases: New paradigms in many-body physics, Adv. Phys. **70**, 1 (2021).

[57] C. Nayak, S. H. Simon, A. Stern, M. Freedman, and S. D. Sarma, Non-Abelian anyons and topological quantum computation, Rev. Mod. Phys. **80**, 1083 (2008).

[58] A. Stern and N. H. Lindner, Topological quantum computation—From basic concepts to first experiments, Science **339**, 1179 (2013).

[59] J. E. Müller, Effect of a nonuniform magnetic field on a two-dimensional electron gas in the ballistic regime, Phys. Rev. Lett. **68**, 385 (1992).

[60] P. D. Ye, D. Weiss, R. R. Gerhardts, M. Seeger, K. von Klitzing, K. Eberl, and H. Nickel, Electrons in a periodic magnetic field induced by a regular array of micromagnets, Phys. Rev. Lett. **74**, 3013 (1995).

[61] J. R. Williams and C. M. Marcus, Snake states along graphene *p-n* junctions, Phys. Rev. Lett. **107**, 046602 (2011).

[62] P. Rickhaus, P. Makk, M.-H. Liu, E. Tovari, M. Weiss, R. Maurand, K. Richter, and C. Schönenberger, Snake trajectories in ultraclean graphene p-n junctions, Nat. Commun. **6**, 6470 (2015).

[63] J. Reijniers and F. M. Peeters, Snake orbits and related magnetic edge states, J. Phys.: Condens. Matter **12**, 9771 (2000).

[64] J. Reijniers, A. Matulis, K. Chang, F. M. Peeters, and P. Vasilopoulos, Confined magnetic guiding orbit states, Europhys. Lett. **59**, 749 (2002).
[65] A. Nogaret, Electron dynamics in inhomogeneous magnetic fields, J. Phys.: Condens. Matter **22**, 253201 (2010).
[66] L. Oroszlány, P. Rakyta, A. Kormányos, C. J. Lambert, and J. Cserti, Theory of snake states in graphene, Phys. Rev. B **77**, 081403(R) (2008).
[67] T. K. Ghosh, A. De Martino, W. Häusler, L. Dell'Anna, and R. Egger, Conductance quantization and snake states in graphene magnetic waveguides, Phys. Rev. B **77**, 081404(R) (2008).
[68] S. Park and H.-S. Sim, Magnetic edge states in graphene in non-uniform magnetic fields, Phys. Rev. B **77**, 075433 (2008).
[69] A. Nogaret, P. Mondal, A. Kumar, S. Ghosh, H. Beere, and D. Ritchie, Crossover between magnetic and electric edges in quantum Hall systems, Phys. Rev. B **96**, 081302(R) (2017).
[70] P. Mondal, A. Nogaret, and S. Ghosh, Quantum transport through pairs of edge states of opposite chirality at electric and magnetic boundaries, Phys. Rev. B **98**, 125303 (2018).
[71] T. Taychatanapat, J. Y. Tan, Y. Yeo, K. Watanabe, T. Taniguchi, and B. Özyilmaz, Conductance oscillations induced by ballistic snake states in a graphene heterojunction, Nat. Commun. **6**, 6093 (2015).
[72] A. Nogaret, S. J. Bending, and M. Henini, Resistance resonance effects through magnetic edge states, Phys. Rev. Lett. **84**, 2231 (2000).
[73] M. Hara, A. Endo, S. Katsumoto, and Y. Iye, Transport in a two-dimensional electron-gas narrow channel with a magnetic-field gradient, Phys. Rev. B **69**, 153304 (2004).
[74] L. Solimany and B. Kramer, Electron in a magnetic quantum dot, Solid State Commun. **96**, 471 (1995).
[75] H.-S. Sim, K.-H. Ahn, K. J. Chang, G. Ihm, N. Kim, and S. J. Lee, Magnetic edge states in a magnetic quantum dot, Phys. Rev. Lett. **80**, 1501 (1998).
[76] J. Reijniers, F. M. Peeters, and A. Matulis, Quantum states in a magnetic antidot, Phys. Rev. B **59**, 2817 (1999).
[77] N. Kim, G. Ihm, H.-S. Sim, and K. J. Chang, Electronic structure of a magnetic quantum ring, Phys. Rev. B **60**, 8767 (1999).
[78] K. W. Murch, K. L. Moore, S. Gupta, and D. M. Stamper-Kurn, Observation of quantum-measurement backaction with an ultracold atomic gas, Nat. Phys. **4**, 561 (2008).
[79] R. Folman, P. Kruger, J. Schmiedmayer, J. Denschlag, and C. Henkel, Microscopic atom optics: From wires to an atom chip, Adv. At., Mol., Opt. Phys. **48**, 263 (2002).
[80] B. T. Seaman, M. Krämer, D. Z. Anderson, and M. J. Holland, Atomtronics: Ultracold-atom analogs of electronic devices, Phys. Rev. A **75**, 023615 (2007).
[81] L. Amico, G. Birkl, M. Boshier, and L.-C. Kwek, Focus on atomtronics-enabled quantum technologies, New J. Phys. **19**, 020201 (2017).
[82] D. Jaksch, Optical lattices, ultracold atoms and quantum information processing, Contemp. Phys. **45**, 367 (2004).
[83] E. T. Jaynes and F. W. Cummings, Comparison of quantum and semiclassical radiation theories with application to the beam maser, Proc. IEEE **51**, 89 (1963).
[84] M. Born and R. Oppenheimer, Zur Quantentheorie de Moleken, Ann. Phys. (Berlin, Ger.) **389**, 457 (1927).
[85] C. A. Mead and D. G. Truhlar, On the determination of Born-Oppenheimer nuclear motion wave functions including complications due to conical intersections and identical nuclei, J. Chem. Phys. **70**, 2284 (1979).
[86] M. V. Berry, Quantal phase factors accompanying adiabatic changes, Proc. R. Soc. London, Ser. A **392**, 45 (1984).
[87] F. Wilczek and A. Zee, Appearance of gauge structure in simple dynamical systems, Phys. Rev. Lett. **52**, 2111 (1984).
[88] J. Moody, A. Shapere, and F. Wilczek, Realizations of magnetic-monopole gauge fields: Diatoms and spin precession, Phys. Rev. Lett. **56**, 893 (1986).
[89] C. A. Mead, Molecular Kramers degeneracy and non-Abelian adiabatic phase factors, Phys. Rev. Lett. **59**, 161 (1987).
[90] *Geometric Phases in Physics*, edited by A. Shapere and F. Wilczek (World Scientific, Singapore, 1989).
[91] C. P. Sun, High-order quantum adiabatic approximation and Berry's phase factor, J. Phys. A **21**, 1595 (1988).
[92] C. P. Sun and M. L. Ge, Generalizing Born-Oppenheimer approximations and observable effects of an induced gauge field, Phys. Rev. D **41**, 1349 (1990).
[93] S. Haroche, M. Brune, and J. M. Raimond, Trapping atoms by the vacuum field in a cavity, Europhys. Lett. **14**, 19 (1991).
[94] V. E. Lembessis, Artificial gauge potentials for neutral atoms: An application in evanescent light fields, J. Opt. Soc. Am. B **31**, 1322 (2014).
[95] M. Mochol and K. Sacha, Artificial magnetic field induced by an evanescent wave, Sci. Rep. **5**, 7672 (2015).
[96] M. Cheneau, S. P. Rath, T. Yefsah, K. J. Günter, G. Juzeliũnas, and J. Dalibard, Geometric potentials in quantum optics: A semiclassical interpretation, Europhys. Lett. **83**, 60001 (2008).
[97] L. D. Landau and E. M. Lifshitz, *The Classical Theory of Fields* (Pergamon Press plc, UK, 1998), Chap. 3.
[98] J. D. Jackson, *Classical Electrodynamics* (Wiley, New York, 1962).
[99] P. Meystre, Velocity dependent spontaneous emission: Strong coupling regime, Opt. Commun. **90**, 41 (1992).
[100] A. Kozlovskii, Photon emission of a two-level atom moving in a cavity, J. Exp. Theor. Phys. **93**, 462 (2001).
[101] X.-L. Qi and S.-C. Zhang, Topological insulators and superconductors, Rev. Mod. Phys. **83**, 1057 (2011).
[102] K. Seo, L. Han, and C. A. R. Sá de Melo, Topological phase transitions in ultracold Fermi superfluids: The evolution from Bardeen-Cooper-Schrieffer to Bose-Einstein-condensate superfluids under artificial spin-orbit fields, Phys. Rev. A **85**, 033601 (2012).
[103] M. Sato, Y. Takahashi, and S. Fujimoto, Non-Abelian topological order in s-wave superfluids of ultracold fermionic atoms, Phys. Rev. Lett. **103**, 020401 (2009).
[104] B. Wu and Q. Niu, Superfluidity of Bose–Einstein condensate in an optical lattice: Landau–Zener tunnelling and dynamical instability, New J. Phys. **5**, 104 (2003).
[105] A. J. Ferris, M. J. Davis, R. W. Geursen, P. B. Blakie, and A. C. Wilson, Dynamical instabilities of Bose–Einstein condensates at the band edge in one-dimensional optical lattices, Phys. Rev. A **77**, 012712 (2008).
[106] S. Slama, S. Bux, G. Krenz, C. Zimmermann, and Ph. W. Courteille, Superradiant Rayleigh scattering and collective

atomic recoil lasing in a ring cavity, Phys. Rev. Lett. **98**, 053603 (2007).

[107] B. W. Shore, P. Meystre, and S. Stenholm, Is a quantum standing wave composed of two travelling waves, J. Opt. Soc. Am. B **8**, 903 (1991).

[108] J. J. Sakurai, *Modern Quantum Mechanics*, revised ed., edited by S. F. Tuan (Addison-Wesley, Reading, Massachusetts, 1994).

[109] F. Nicacio and F. L. Semiao, Coupled harmonic systems as quantum buses in thermal environments, J. Phys. A **49**, 375303 (2016).